Au nanocluster coupling with Gd-Co$_2$B nanoflakes embedded in reduced TiO$_2$ nanosheets: Seawater electrolysis at low cell voltage with high selectivity and corrosion resistance

Tanveer ul Haq [a], Mujaheed Pasha [b], Yongfeng Tong [b], Said A. Mansour [b], Yousef Haik [c],*

[a] *Sustainable Energy Engineering, Frank H. Dotterweich College of Engineering, Texas A&M University, Kingsville, TX 78363-8202, USA*
[b] *Qatar Energy and Environment Research Institute, Hamad bin Khalifa University, Qatar Foundation, 34110 Doha, Qatar*
[c] *Department of Mechanical and Industrial Engineering, Frank H. Dotterweich College of Engineering, Texas A&M University, Kingsville, TX 78363-8202, USA*

A B S T R A C T

Seawater electrolysis offers a promising technology for environmental remediation and mass production of sustainable hydrogen. However, intricated synthetic routes, limited oxygen selectivity, and electrode corrosion severely hamper the practical viability of this technology. Here, we designed an effective strategy to assemble interface-rich, Au NCs decorated Gd-Co$_2$B nanoflakes embedded in TiO$_2$ nanosheets grown on Ti foil (Au-Gd-Co$_2$B@TiO$_2$) to meet the multiple needs of electrodes for seawater electrolysis. Benefiting from the high electrical conductivity, superior intrinsic activity, and improved transfer coefficient, this free-standing, Au-Gd-Co$_2$B@TiO$_2$ electrocatalyst demonstrates outstanding performance towards overall seawater splitting needing a small over-potential of 510 mV to attain a geometric activity of 1000 mAcm^{-2} in alkaline seawater. The higher activity and specificity of Au-Gd-Co$_2$B@TiO$_2$ are credited to the oxygen vacancies and the presence of the Co-Au surface. Furthermore, its super hydrophilic-aerophobic features, improved corrosion resistance, and impressive durability reveal its practical viability for actual seawater electrolysis.

1. Introduction

The rapid depletion of fossil fuels and their drastic effect on the environment is considered one of the most severe threats to human society. Exploration of renewable energy resources provides alternative pathways for producing clean, cheap, and abundant energy to sustain our future generations. Hydrogen is an ideal fuel due to its high energy density and zero carbon emission characteristics (water being the sole byproduct) [1]. Water electrolysis offers a reliable path to convert water into hydrogen and oxygen without any obnoxious byproduct. Generally, water electrolysis needs ultra-purified water in various modules, including anion exchange membrane water electrolyzers (AEMWE), proton exchange membrane water electrolyzers (PEMWE), and alkaline water electrolyzers (AWE) [2]. In contrast, for the deployment of large-scale electrolyzers, see water electrolysis is the promising option for the large-scale production of H$_2$, decreasing the cost and significantly reducing the complex set up of electrodes. Direct electrolysis of seawater in water splitting configurations is challenging due to the variety of dissolved ions that can disturb the catalytic system. Their average molar

concentration is ~0.599 m, corresponding to an average global salinity of ~3.5% [3]. Dissolved ions in the electrolyte may kill or accelerate the degradation of the electrocatalyst through the formation of different complexes at both anode and cathode. Even more conceding to the operation of a seawater system is that anions, i.e., chloride, give rise to undesired rival electrochemical reactions at the anode on their corresponding anodic potential, delivering undesired side products chlorinated oxidants or molecular chlorine [3].

The major challenge in seawater splitting is the competition between OER and chloride anion chemistry at the anode due to their close redox potential. The electro-oxidation chemistry of Cl is complicated due to its multistep and high dependency on pH, applied potential, and Temperature. The chlorination process involves the formation of various pH-dependent intermediates. Lower pH value (pH < 3) favors the free chlorine evolution reaction (ClER) due to privileged adsorption of Cl$^-$ species over oxygen-containing intermediates, while hypochlorous acid formation becomes the major reaction for pH 3–7.5. Similarly, hypochlorite formation occurs at pH values higher than 7.5, representing the pKa of hypochlorous acid [4]. The chloride oxidation reaction at two

extreme pH values is:

$$2Cl^- \rightarrow Cl_2 + 2e^- \text{ (ClER, E = 1.36 V vs RHE, pH = 0)}$$

$$Cl^- + 2OH^- \rightarrow ClO^- + H_2O + 2e^- \text{ (Hypochlorite formation, E = 1.71 V vs RHE, pH = 14)}$$
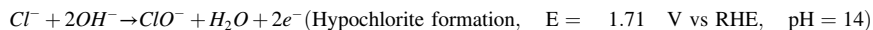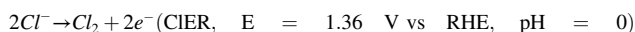
The ClER relatively follows a simple mechanism, and its kinetics involves the transfer of 2 electrons. A serious challenge, however, is the slow rate of multistep OER, which requires high activation energy and thus large overpotential to break the O–H bond and to form an O–O bond and transfer 04 electrons essentially required for oxygen evolution from two water molecules at the same time. Other challenges include the presence of non-innocent ions (both anions and cations), bacteria/microbes, and small particulates present in seawater, which may not only decline/poison electrodes/catalysts performance and long-term stability but also dissolve the membranes used for the separation of the anode and cathode [5].

Recently researchers have established several strategies to enhance the selectivity of anode materials for OER that operate in saline or low-grade water, i.e., (I) to optimize the surface free energy of active sites that selectively bind with the oxygen-containing intermediates either in an acidic or basic environment [6]. The binding affinity of metal surface for OOH intermediate can be increased through selective metal doping with lower d electrons than the host cation [7]; (II) to maximize the thermodynamic potential difference between the two electrochemical processes by performing the electrolysis in basic conditions [5]. This infers the development of highly efficient anode materials that deliver the desired TON at an overpotential of less than 480 mV (equilibrium potential for hypochlorite formation). So, it needs to accelerate the OER process before the chlorination reaction at low overpotential ($\leq$ 480 mV), known as the 'alkaline design criterion' in saline water electrolysis. It is often difficult to achieve the high geometric activity below an overpotential of 480 mV.

Transition metal borides (TMB) have outstanding mechanical stability and corrosion resistance and have revealed excellent stability for seawater electrolysis [8,9]. Although, most reported TMB parade reasonable OER and HER activity, optimization strategies, such as alloying, electronegative metal doping (having lower d electrons), interface, and vacancy engineering, further ameliorate their activity, selectivity, and durability for seawater electrolysis [10]. Recent works have unveiled that Au atoms can effectively ameliorate the electronic conductivity of TM due to its predilection interfacial interactions. Au, though, is expensive, but even its small percentage ($<$ 1%) in a hybrid material could transfer electrons at the interface, changing the charge distribution, which is highly beneficial in water splitting catalysis. This ameliorated activity after incorporating Au has been proposed due to several possible reasons, including synergistic effect, fast rate of electronic transportation at interface boundary, redox couple of $Au^{0/1+}$, and preferential formation of OOH intermediates [11]'. Recently, Thomas F. Jaramillo et al. have inspected that Au dispersion on metal oxide enhanced the geometric activity compared to their non-Au counterpart [12].

Similarly, Zhen Zhou reported that Au- metal-oxide interface decreases the adsorption free energy of the OOH intermediate and uplifts the potential determining step from M-O to MOOH [13]. In another report, it has been justified that Au can promote the MOOH bond formation on the surface of transition metals [14]. Usually, aggressive treatment such as thermal heating creates a metal support interaction that triggers the sintering and minimizes metal atoms' usage efficiency [15]. A key challenge is the uniform dispersion of ultra-small Au clusters

on TM with minimum weight percentage but maximum exposure of active sites in terms of their redox couple and sustain compositional, structural, and mechanical stability.

Considering the need for electrocatalyst with high-density active sites and large surface area for selective seawater electrolysis, here we report a synthesis of Au NCs loaded on Gd- Co_2B nanoflakes, which were grown on both side of conductive r-TiO$_2$ nano sheet (NS) arrays, that shows the following advantageous concurrently: (I) The r-TiO2 NS with large surface area and excellent corrosion resistance serve as a strong skeleton and the anticorrosive Gd- Co_2B nanoflakes role as a strong armor, cooperatively contributing to good stability against the aggressive seawater. (2) The partial oxidation of Co through Au doping stabilizes the OOH formation, thereby facilitating OER over chlorine species formation reaction [4]. (3) Both the Co_2B and Au are highly conductive, which promises efficient charge transfer between the catalyst surface and seawater, thus boosting the water splitting kinetics at low overpotential. In addition, the electrons of the unfilled 4f orbitals of Gd could abide in the hyper 5d orbitals and thus go into valance electrons, which indorses electronic conduction [16]. (4) The effective microwave heating creates a strong interaction between Au and Gd-Co_2B@TiO$_2$ nanoflakes indorse the structural and mechanical stability due to synergistic promotions.

The synthesized Au-Gd-Co_2B@TiO$_2$ catalyst yields high geometric activity of 2A at an overpotential of 370 mV and 290 mV for OER and HER, respectively, in 1 M KOH seawater. The geometric activity of 1 A/cm^2 is attained at a record low voltage of 1.74 V in 2 electrode setup using Au-Gd- Co_2B @TiO$_2$ as both anode and cathode and sustain for continuous 200 h without hypochlorite formation. We believe this work significantly boosts the technology of seawater electrolysis.

2. Experimental section

2.1. Chemicals and materials

Titanium foil (0.25 mm, Sigma Aldrich), Chloroauric acid (HAuCl$_4$, $\geq$ 98%, Sigma Aldrich), Gadolinium Chloride (GdCl$_3$ $\geq$ 98%, Sigma Aldrich), Cobalt nitrate hexahydrate (Co (NO$_3$)$_2$·6H$_2$O, $\geq$ 98%, Sigma Aldrich), Ruthenium oxide (RuO$_2$, 99%, Sigma Aldrich), Pt/C (Sigma Aldrich), Urea (CH$_4$N$_2$O, Sigma Aldrich), Boric acid (H$_3$BO$_3$, Alfa Aesar), Sodium Borohydride (NaBH4, Powder $>$ 99%, Sigma Aldrich), Sodium chloride (NaCl, Sigma Aldrich), Sulfuric acid (H$_2$SO$_4$ $\leq$ 98%, Sigma Aldrich), Potassium hydroxide (KOH, $\geq$ 95%, Sigma-Aldrich), Sodium hydroxide (NaOH, $\geq$ 95%, Sigma-Aldrich), Hydrochloric acid (HCl, 37%, Alfa Aesar), Ethanol (C$_2$H$_5$OH, $\geq$ 98%, Sigma Aldrich), Methanol (CH$_3$OH, $\geq$ 98%, Sigma Aldrich), Isopropanol ($\geq$ 98%, Sigma Aldrich). Milli-Q ultrapure water with resistance of 18 M Ω cm^{-1} was used throughout this study.

2.2. Synthesis of porous TiO$_2$ nanosheets

r-TiO$_2$ nanosheets were directly grown on Ti foil through a hydrothermal reaction in alkaline solution. Typically, a Ti foil with size (3 * 3 in.) was first ultrasonically washed by using ethanol, acetone, isopropanol, and DI water to eliminate the surface contamination and finally dried in an Ar gas flow. In a hydrothermal process, Ti foil was put vertically into 50 ml stainless steel autoclave holding 25 ml NaOH solution. The sealed autoclave was placed in preheated electric oven at 180 °C for various times. The Na$_2$Ti$_3$O$_7$ morphology and surface structure can be optimized by varying the hydrothermal parameters. After

hydrothermal process, $Na_2Ti_3O_7$ nanosheets were impregnated in 1 M HCl solution, that allow the thermodynamically favorable ion exchange process for the development of $H_2Ti_3O_7$ nanostructure. Finally, this sample was washed with DI water and IPA and calcinated at 550 °C for 2 h for the fabrication of TiO_2 nanosheets on Ti foil.

2.3. Synthesis of Gd-Co_3O_4 nanoflakes @ TiO_2 nanosheets

Gd-Co_3O_4 nanoflakes was electrochemically deposited on TiO_2 using standard three electrode setup, while using TiO_2 nanosheets @Ti Foil, graphite rod, and Ag/AgCl as working, counter, and reference electrode, respectively. To eliminate the probability of metal contamination, the electrochemical cell, counter, and reference electrodes were washed with 50% HCl. To prepare the electrolyte for electrochemical deposition process, 50 mM Co $(NO_3)_2$, 10 mM $GdCl_3$, 20 mM urea and 20 mM boric acid were dissolved in 40 ml of ethanol. Initially, 2 cycles were performed in absolute ethanol from 0.75 to 2 V vs RHE and then chronopotentiometry was done in electrolyte (containing equal volume of above listed precursors) at constant current density 0f$-$1 mA/cm^2 for 2,4,6,8 and 10 minutes. Initially, rapid enhancement in potential was observed within 2 min after that it goes to steady state position. The Gd and Co stoichiometry were controlled just by changing the Gd and Co ratio.

2.4. Synthesis of Gd-Co_2B nanoflakes @ TiO_2 nanosheets

To modify the surface of Gd-Co_3O_4 nanoflakes embedded in r-TiO_2 nanosheets, the free standing Gd-Co_3O_4@TiO_2 precursor was dipped in 0.1 M $NaBH_4$ aqueous solution at room temperature for 30 min. As $NaBH_4$ serve as "B" source and reducing agent in this reaction, the NaOH solution (0.2 M) was also added to decelerate the $NaBH_4$ hydrolysis. After this chemical reduction, Gd-Co_2B@TiO_2 self-supported electrode were dried in a vacuum oven.

2.5. Synthesis of Au-Gd-Co_2B nanoflakes @ TiO_2 nanosheets

Radio frequency magnetron sputter was used for the direct deposition of ultrasmall Au NCs on Gd-Co_2B nanoflakes @ TiO_2 nanosheets film using Au target (99.99% pure, d = 19.30 g/cm^3, Melting point 1064.18 °C, Cp 25.418 J mol^{-1} K^{-1}). The deposition was performed at room temperature on a dry substrate (Gd-Co_2B nanoflakes. The base pressure was < 2×10^{-6} torr and the sputtering duration was just 3 s. The distance between substrate and the Au target was 20 cm. The support was rotated at constant angular frequency during deposition to ensure the uniform nucleation and growth of Au NCs.

2.6. Microwave treatment

In order to create a strong interaction between ultrasmall Au NCs and Gd-Co_2B@TiO_2, microwave radiations were employed. The freestanding Au-Gd-Co_2B@TiO_2 catalyst was kept under microwave radiation in ethylene glycol at 200 °C with a ramp time of 3 min and a hold time of 2 min.

2.7. Synthesis of IrO_2 and Pt/C catalyst on Ti foil

The IrO_2 anode and Pt/C cathode were developed on Ti foil for comparison in this experiment. The slurry was made by dispersing 40 mg of IrO_2 in a solution containing 0.5 ml ethanol, 0.4 ml DI water and 0.05 ml Nafion. The slurry was then spin coated on Ti foil, dried in vacuum at 60 °C for 2 h. The Pt/C cathode was acquired by same procedure.

2.8. Structural and chemical characterizations

The surface structure and morphological features of all the synthesized catalysts were analyzed by using scanning electron microscope (JEOL 7800, Oxford EDS) and Transmission electron microscopy (FEI-Thermo scientific- TALOC C). Elemental composition was carried out by using (FEI-Thermo scientific- TALOC C) with a 7 kV beam voltage. Atomic force microscopy (AFM, Bruker Dimension edge Scientific) was used to probe the sheet thickness and surface roughness. X-ray photoelectron spectroscopy XPS (Thermo scientific – ESCALABZ 50i) was conducted to probe the elemental composition and surface environment of synthesized catalyst. Survey XPS spectra were obtained in a binding energy range from 0 to 1300 eV. The binding energy of the peaks were calibrated to that of the adventitious carbon at 284.5 eV.

2.9. Electrochemical characterizations

Electrochemical measurements of these as-prepared catalysts were performed on a Gamry Reference 3000 electrochemical station using a three-electrode setup. The as prepared catalyst, Hg/HgO and graphite rode were used as working, reference and counter electrodes, respectively.

The cyclic polarization curve of each catalyst was conducted at low scan rate (1 mV/s) with 10% iR compensation. Initially 20 cycles were performed for each catalyst to stabilize the active sites. All the potentials were calibrated to the reversible hydrogen electrode using the equation: E $_{RHE}$ = E $_{Hg/HgO}$ + 0.098 V + 0.059 PH. The Tafel slope was determined by $\eta = a + b \log (j)$, where j represent the current density. The electrochemical impedance spectroscopy (EIS) calculations were completed under the similar conditions at an overpotential near to onset potential from 10^6 to 10^{-1} Hz with an A.C voltage of 5 mV/s. Seawater was collected from Corpus Christi-Texas, USA, and used without any treatment. The alkaline seawater was made by adding potassium hydroxide (KOH) to the seawater until the pH of the solution reached 13. The white insoluble precipitate was observed and filtered by centrifugation.

2.10. Theoretical method for OER

The Jan Rossmeisl and his coworker mechanism (adsorbate evolution mechanism) was considered for the theoretical estimation of OER [17]. The reaction free energy for each intermediate could be stated as follow:

$$\Delta G_1 = E(OH^*) - E(*) - EH_2O + 1/2E_{H_2} + (\Delta ZPE\text{-}T\Delta S) - eU$$

$$\Delta G_2 = E(O^*) - E(OH*) + 1/2E_{H_2} + (\Delta ZPE\text{-}T\Delta S) - eU$$

$$\Delta G_1 = E(OOH^*) - E(O*) - EH_2O + 1/2E_{H_2} + (\Delta ZPE\text{-}T\Delta S) - eU$$

$$\Delta G_1 = E(*) - E(OOH^*) - EO_2 + 1/2E_{H_2} + (\Delta ZPE\text{-}T\Delta S)\text{-}eU$$

Where ΔG_1, ΔG_2, ΔG_3, and ΔG_4 are the Gibbs free energy of each step, while E (*), E(OH*), E(O*), and E(OOH*) are the total energy of the pristine surface and OH, O and OOH intermediate adsorbed on the surface. The computational vibration frequency estimated the ΔZPE values. The term TΔS represents the entropic factor, and eU is the external potential enforced on each step.

3. Result and discussion

3.1. Preparation

An alkaline hydrothermal process was used to grow TiO_2 nanosheets on the surface of Ti foil. It is generally recognized that alkaline treatment of Ti foil causes delamination into $Na_2Ti_3O_7$ nanosheets intermediates which are finally transformed to TiO_2. Ion exchange reaction with HCl was performed to replace Na^+ with H^+ as $Na_2Ti_3O_7$ cannot be directly converted into TiO_2. During pyrolysis at high temperatures (500 °C), $H_2Ti_3O_7$ will be dehydrated and induce the formation of TiO_2
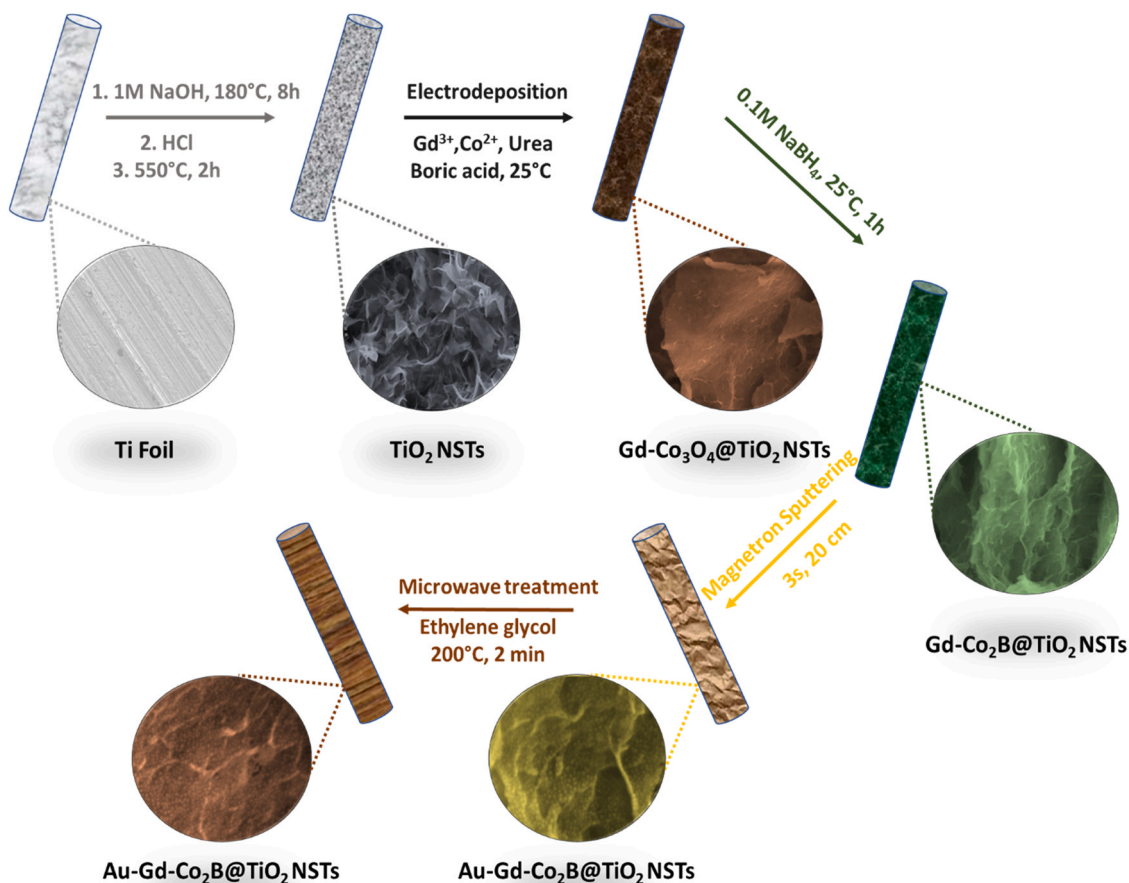
Scheme 1. Systematic illustration of the fabrication of Au-Gd-Co$_2$B@TiO$_2$.

nanostructure. The structural features of initial Na$_2$Ti$_3$O$_7$ nanostructures are well preserved during the phase transition process (Fig. S1). It was also observed that NaOH concentration has a substantial impact on the morphology of TiO$_2$ nanostructure (Fig. S2). A constant current density strategy enabled the development of Gd-Co$_3$O$_4$ nanoflakes from a metal salt solution, as shown in Scheme 1. The TiO$_2$ nanosheets are used as a substrate that provides a high surface area for the fabrication of bimetallic catalysts. Urea, a homogenous precipitation agent, was used for diffusion-controlled growth [18]. During the cathodic deposition process, urea is decomposed into NH^{4+}, CO$_3^{2-}$ and OH$^-$, increase the pH in the vicinity of the electrode surface and persuading the deposition/precipitation of metals. Initially, a sharp increment in cathodic potential was observed that probably due to the deposition of Co (Co^{2+}(aq) + 2e$^-$ → Co (s)E^o(V) = − 0.28). Initially. Gd^{3+} ions remain inactive due to its low reduction potential, Gd^{3+}(aq) + 3e$^-$ → Gd (s)E^o(V) = −2.279) and sustaining the same concentration across the electrolyte. However, the unceasing increment in the cathodic potential indorse the effective deposition of bimetallic nanoflakes (Fig. S3) [19]. It was inspected that different independent variable, e.g., applied potential, precursor concentration, and reaction time, substantially impact nanoflakes' surface structure (Fig. S4). In the subsequent chemical reduction step, various Gd-Co$_2$B samples were attained by dipping Gd-Co$_3$O$_4$ precursor in NaBH$_4$ aqueous solution at room temperature for 30 min. The pH of the solution decrease when Cobalt oxide reacts with the BH$_4^-$ and releases vigorous H$^-$ ions. When sufficient cobalt oxide reduces, the pH increases swiftly as now the primary reaction is the hydrolysis of NaBH$_4$. Researchers demonstrated that the B content in the vicinity of Co has a linear relation with the BH$_4^-$ concentration. The hydride ions (H$^-$) released from NaBH$_4$ and reveals a strong reducing ability can act as an oxygen scavenger to generate oxygen defects and modify the structure of Gd-Co$_3$O$_4$ bimetallic film [20].

$$4BH_4^- + 2Co^{2+} + 9H_2O \rightarrow Co_2B + 3B(OH)_3 + 12.5H_2$$
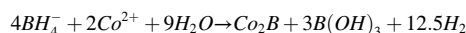
The SEM images demonstrated that the Gd-Co$_2$B sample has a more porous and thinner nanoflake structure than Gd- Co$_3$O$_4$ (Fig. S5). This external chemical reduction step can intensively enhance the uncoordinated surface area and increase the activity of active sites [21]. Ultrasmall Au NCs were deposited on the surface of Gd-Co$_2$B nanoflakes through a scalable vapor deposition method. RF power and total pressure are the critical parameters of vapor phase deposition. High RF power increases the collision frequency both in the plasma phase and during the growth of nanostructure. The size and structure of Au NCs were controlled by optimizing the RF Power, deposition time, pressure, and the distance between substrate and Au target. The SEM images revealed that ultrasmall NCs are homogeneously dispersed on the surface of Gd-Co$_2$B@TiO$_2$ (Fig. S6). As gold is highly electronegative (2.54), it can withdraw the electronic density from Co (1.88) and ensure electron-deficient Co species [22].

For the Au NCs, it is supposed to be a challenge to create a strong interaction with the underlying support because of Au's low surface energy and wok function (Fig. S7) [23]. This weak interaction leads to a catalyst's deactivation, which results from metal sintering and surface area loss. We addressed this problem by demonstrating a strong interaction between Au NCs and Gd-Co$_2$B@TiO$_2$ via microwave-assisted heating in ethylene glycol (EG) solvent. The EG is a good MW absorbent and facilitates efficient heating due to its high loss tangent value (tan δ = 1.350) (Table S1) [24]. This post-heating process does not impart any considerable impact on the surface chemistry of synthesized catalysts.
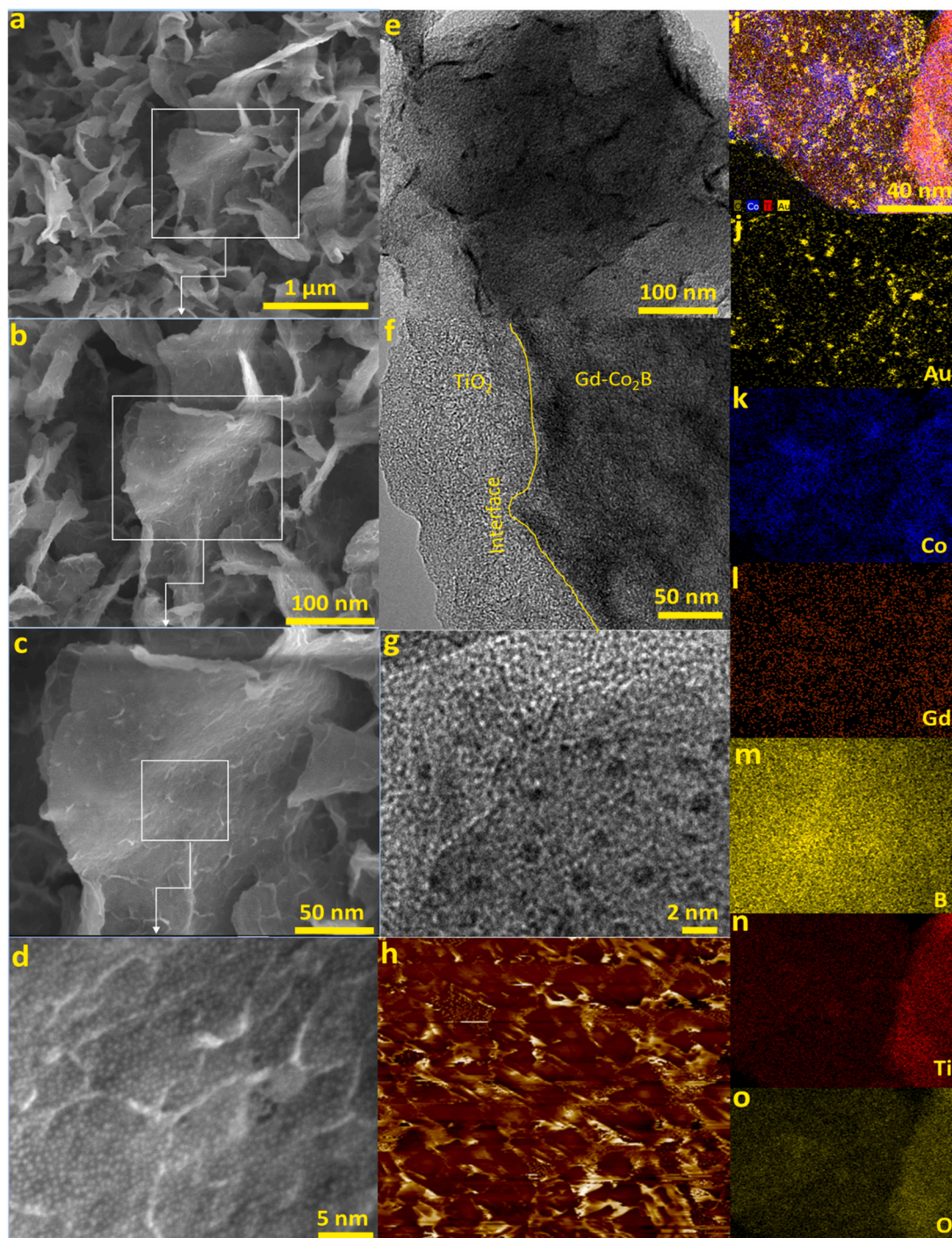
Fig. 1. (a–d) SEM, (e, f) TEM, (g) HRTEM, (h) AFM, (i) STEM images and (j–o) corresponding elemental mapping for Au-Gd-Co$_2$B@TiO$_2$.

3.2. Characterization

The scanning electron microscopy (SEM) images in Fig. S8 reveal that the Ti foil has a clean surface. After hydrothermal reaction for 6 h in NaOH, its surface is uniformly covered by a randomly aligned nanosheets array, and no exposed surface of Ti foil was observed (Fig. S8). The magnified images show that TiO$_2$ nano sheets are directly grown from the Ti foil and show strong interface contact (Fig. 1). The transmission electron microscopy (TEM) images further expose the thin and smooth surface of TiO$_2$ sheets (Fig. S9). The high-resolution transmission electron microscopy (HRTEM) images demonstrate the lattice fringes with an interplanar spacing of 0.19 nm, which is qualified for the

(200) plane of TiO$_2$ (Fig. S10) [25]. After cathodic deposition with Gd and Co precursor, Gd- Co$_2$B@TiO$_2$ parades a well-preserved nanosheets array morphology. The SEM images in Fig. 1(a–c) demonstrate that Gd-Co$_2$B nanoflakes were intersected with each other on TiO$_2$ sheets to form a 3D hierarchical structure with abundantly void spaces. These micro-voids among the nanoflakes contribute towards a porous assembly, which benefits seawater diffusion and gas bubble discharging [26]. The SEM images of Gd- Co$_3$O$_4$ and Gd-Co$_2$B in Fig. S5 validate that their structure could be slightly modified after the boronization step, while the intersected structure was well retained. Further, the high magnification SEM images reveal that the Gd-Co$_2$B nanoflakes thickness is in the range of 1–2 nm. It was observed that specific stichometry of Gd has a

prime role in the development of nanoflake structures (Fig. S11). Fig. 1e expresses a TEM image of Au-Gd-Co$_2$B@TiO$_2$ single sheets revealing a dense surface with ultrasmall Au NPs attached. Fig. S9 shows the TEM image of Au NPs stripped from the Au-Gd-Co$_2$B nanosheets, in which the NPS with ultra-small sizes are well dispersed on Gd-Co$_2$B@TiO$_2$, recommending that vapor deposition is an effective strategy to synthesize the highly disperse NCs without any capping agent. The TEM images signpost the highly uniform Au NPs with a mean diameter of 1–2 nm (Fig. 1 g). This ultrasmall size enlarges the electrochemical active surface area (ECSA) and increases the reaction rate. The SEM images of Au-Gd-Co$_2$B@TiO$_2$ recorded after microwave heating indicate that this treatment has no impact on the size and topography of the catalyst (Fig. S12). The amorphous nature of Gd-Co$_2$B has the advantage of flexibility which allows the catalyst to self-regulate according to the seawater and offer means for both surface and volume confined electrolysis [27]. Fig. 1(i-o) represents the EDS elemental mapping images of Au, Co, Gd, B, Ti, and O, further verifying the NPs decorated flake's structure embedded in nanosheets as well as confirming the presence and uniform distribution of six elements. Surface morphology and thickness of nanosheets are observed under the atomic force microscopy (AFM) technique, which advocates that a layer structure of TiO$_2$ is formed. These continuous TiO$_2$ layers are shaped by a single small structure with a tip radius of 5 nm. Fig. 1 h provides an AFM image of the Gd-Co$_2$B nanoflakes embedded in TiO$_2$ sheets with Au NCs grown on them. The AFM image demonstrates the small Au NCs with a diameter around 2 nm due to the flat surface morphology of nanosheets (Fig. S13). It also shows the close packing of nanoflakes embedded in TiO$_2$ sheets and the high roughness of composite material that is required for fast kinetics [28].

The Crystalline structure and phase purity of synthesized catalyst was probed with X-ray diffraction analysis (XRD) (Fig. S14). The sample before calcination shows a diffraction peak at 2θ = 35°, 38°, 41°, 53°, 71.02°, 76.2°, and 77.5° correspond to (100), (002), (101), (102), (103), (112) and (201) reflection plane that almost matches with the diffraction pattern of Ti foil. After heating treatment, new peaks appear at 2θ = 27.4°, 35.9°, 41.1°, 54.3°, 56°, 62.7°, 64.2°, and 69.1° correspond to the lattice planes of (110), (101), (111), (211), (220), (002), (310) and (300) exactly match with rutile phase of TiO$_2$ (JCPDS 73-1764). In addition, a small peak at 2θ = 25.3° and 48.1° corresponds to the (101) and (002) planes of the anatase phase [29].

The spurr equation was used to probe the quantity of anatase in each of the samples

$$F_r = \frac{1}{1 + 0.8\left[\frac{I_A(101)}{I_R(110)}\right]}$$

The intensity of main rutile (110) and anatase (101) peaks was used to find the faction of anatase in a sample. The wight percentage for anatase and rutile compositions is 7:93. The sample after Gd-Co$_3$O$_4$ deposition and boronization (Gd-Co$_2$B@TiO$_2$) does not show any additional peak validating the amorphous structure of the material.

We further performed X-ray photoelectron spectroscopy (XPS) to determine the catalyst's elemental composition, chemical environment, and valance state. Fig. S15 illustrates the survey scan spectra of 2 catalysts, confirming the presence of Au, Gd, Co, Ti, and O in the Au-Gd-Co$_3$O$_4$@TiO2; and Au, Gd, Co, Ti, O, and B in the Au-Gd-Co$_2$B@TiO$_2$, which agree well with the EDS results (Fig. S16). The high-resolution Ti 2p spectra for Au-Gd- Co$_3$O$_4$@TiO$_2$ are shown in Fig. 2a. The less intense peak around 455.9 eV followed by an intense peak at 458.3 eV reveal that the Ti 2P$_{3/2}$ curve can be deconvoluted into two peaks with a correlation coefficient of 0.98. The same pattern is also observed for the Ti 2P$_{1/2}$ component. The peaks at 456 and 458 eV are traits of 3+ and 4+ valance states, respectively. The Ti 2P$_{3/2}$ pattern after the chemical reduction step (treatment with NaBH$_4$) demonstrates an upsurge in the intensity of the 3+ valance state peak that confirms the surface
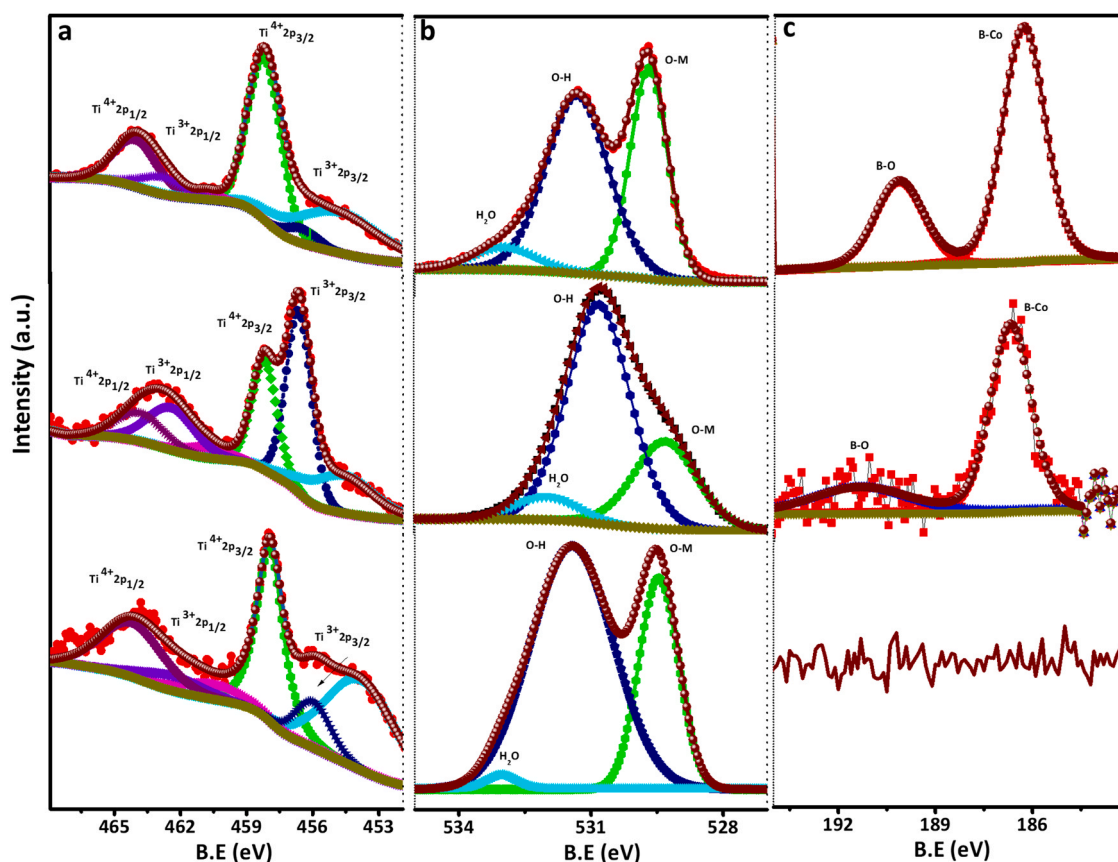

Fig. 2. High resolution XPS spectra of (a) Ti 2p, (b) O 1s, (c) B 1s for Au-Gd-Co$_2$B@TiO$_2$, Gd-Co$_2$B@TiO$_2$ and Gd-Co$_3$O$_4$@TiO$_2$ (from top to bottom).

reduction of TiO_2 nanosheets [30]. These results unveiled that Ti is present abundantly in 3+ valance state in Au-Gd-Co_2B@TiO_2 sample that enhanced its hydrophilicity. Recent findings have established that hydrophilic surface features of the substrate are usually helpful in easier gas bubble releases and for kinetics of electrolyte diffusion during water electrolysis [31]. The primary binding energy for Ti $2P_{3/2}$ and Ti $2P_{1/2}$ shifts towards a little negative value after $NaBH_4$ treatment that shows the alteration in the chemical environment of TiO_2. The O 1s spectra presented the sign for the presence of oxygen vacancies in the Au-Gd--Co_2B@TiO_2 catalyst. The O 1s core-level spectrum is asymmetrical with a tail extending towards the higher energies and deconvoluted into three peaks (Fig. 2b). The peaks at 526, 527, and 529 eV are assigned to the lattice oxygen, OH species, and the oxygen atom of the adsorbed water molecule [32]. The atomic ratio of O/Ti = 1.24 in Au-Gd-Co_2B@TiO_2 appears to be much lower than the stoichiometric ratio O/Ti = 2 in Au-Gd-Co_2B@TiO_2, representing the existence of abundant oxygen vacancies.

In addition to a pair of satellite peak, the core level XPS spectra of Co 2p for Gd- Co_3O_4@TiO_2 can be deconvoluted into two pairs of spin-orbit doubled positioned at binding energy of 778.2 eV and 793.2 eV assigned to Co^{3+} 2p $_{3/2}$ and Co^{3+} $2p_{1/2}$ and the other at 786 and 804.3 eV attributed to $Co^{2+}2p_{3/2}$ and $Co^{2+}2p_{1/2}$ respectively (Fig. 3a). These data have been fitted in consensus with the approach adopted by Biesinger et al. for determining the valance state in XPS spectra of Co hydroxide and oxide [33]. The relative peak intensity and weak satellite peak demonstrate that Co is present abundantly in (3+) valance state [34]. After chemical treatment of Gd- Co_3O_4@TiO_2 with $NaBH_4$, the B.E of Co $2p_{3/2}$ shift to a lower value by 0.29 eV, and B 1s B.E was positively shifted by 0.7 eV relative to the B.E of pure B suggesting that the elemental B is chemically bonded with the Co and not present in the free

state. The partial transfer of electrons from B 2p orbital to Co d orbital due to hybridization creating the electron-dense surrounding around the metal. More crucially, after $NaBH_4$ treatment, Co $^{2+}$/Co^{3+} ratio is increased from 3.04 to 3.21, and the O/Co ratio decreased from 1.78 to 1.16, which signpost the electronic interaction between Gd- Co_3O_4 and B and cause the reactivity alteration across the interface. This electronic interaction is thermodynamically possible due to the high positive surface energy of nanosized Co and high electronegativity of B [35].

Similarly, the B 1s XPS signal is absent in the Gd- Co_3O_4 plot, but it visibly appears in the Gd-Co_2B plot. The high-resolution B 1s spectra of Gd-Co_2B shown two peaks, one at low B.E (187.8 eV) that correlate with Co-B, and the other at higher B.E to B-O (192 eV) (Fig. 2c) [36]. The detected B-O peak should come from the catalyst surface oxidation during atmospheric exposure. The positive shift (0.7 eV) in the binding energy of B in Co_2B structure compared to elemental B endorsed the electronic density migration from B to unfilled d orbital of Co. The antibonding states are less filled for Co_3O_4 (p-type Transition metal oxide) because the highest occupied d state is much closer to the Fermi level and facilitate this reverse electron transfer. As inferred from the peak area, the $NaBH_4$ treatment decreases the O/Co ratio suggesting the formation of higher unsaturated metal cations (surface oxygen deficiency), improves the intermediate adsorption strength on the Co surface, and enhances the surface reactivity [37]. The Gd valance state was investigated by the high-resolution XPS spectrum of Gd 4d. The characteristics peaks at 141.7 and 147.7 eV were observed and attributed to the Gd 4d $_{5/2}$ and Gd 4d $_{3/2}$ of the Gd^{3+} state (Fig. 3b). Gd 4d core-level spectra show multiple splitting originated from the interaction between 4d holes and $4f^7$ valance electrons that form the final 7D and 9D ionic states [38]. The binding energy and splitting pattern signpost the 3+ valance state of Gd compatible with the reported results. After $NaBH_4$
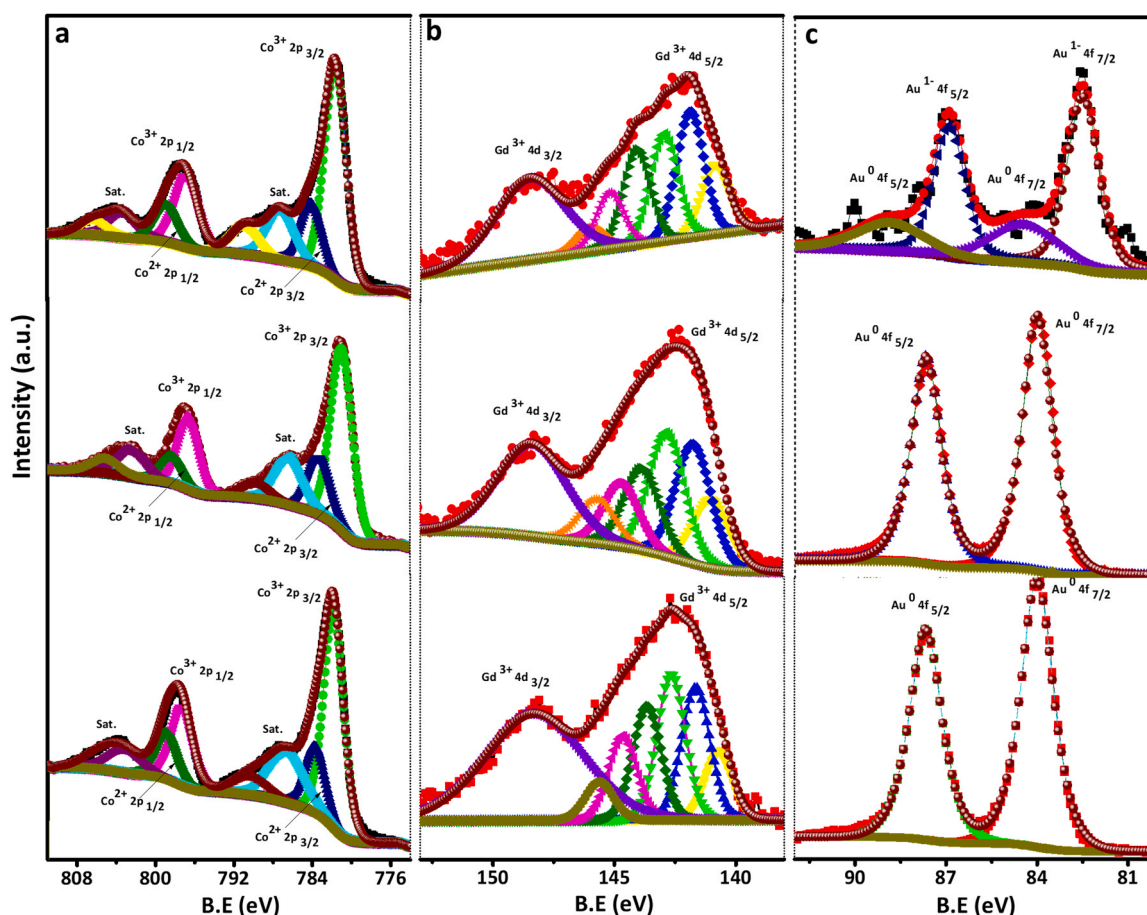

Fig. 3. High resolution XPS spectra of (a) Co 2p, (b) Gd 4d, (c) Au 4f for Au-Gd-Co_2B@TiO_2, Gd-Co_2B@TiO_2 and Gd-Co_3O_4@TiO_2 (from top to bottom).

treatment and loading of Au NCs, the Gd 4d B.E is slightly shifted towards the higher value that validates Gd and Au's electronic interaction.

The Au 4f deconvoluted spectrum show two pairs of spin-orbit coupling demonstrating the presence of Au^0 with two peaks at 83.2 eV and 86.7 eV for Au^0 4f $_{7/2}$ and Au $4f^0$ $_{5/2}$ respectively with a splitting factor of 3.7 e V (Fig. 3c) [39]. The negative B.E energy of Au as compared to previously published results, the appearance of new peak (Co^{3+}) and positive shift in the B.E of Co 2p spectra endorse the electronic shifting from highest occupied molecular orbital (HOMO) of Co to lowest unoccupied molecular orbitals (LUMO) of Au due to electron-withdrawing nature of Au [40].

From all of the above analysis, it is concluded that ultra-small Au NCs modified, Gd-Co_2B nanoflakes embedded in TiO_2 sheets can be attained via a scale-able cathodic deposition followed by a physical vapor deposition process. The SEM, TEM, and AFM analysis demonstrate the homogenous dispersion of Au NCs, high compactness, and interfacial contact between Gd-Co_2B nanoflakes and TiO_2 nanosheets that increase the chemical and mechanical resistance against aggressive seawater. In depth, the XPS study confirms the intermetallic formation responsible for the modification in the coordination and bonding properties and promisingly favorable for selective seawater electrolysis. It was noted that chemical reduction, vapor deposition, and microwave heating have

no considerable impact on the surface structure of synthesized composite; however, both boronization and Au loading change Co's valance state. It reveals that these processes increase the conductivity and number of active sites and enhance the activity, selectivity, and durability of active sites for complex seawater electrolysis.

3.3. Electrochemical activity

The OER activity of as-prepared catalysts was accessed in three types of electrolytes (1 M KOH, 1 M KOH+0.5 M NaCl and 1 M KOH seawater), respectively, at room temperature. All polarization curves were recorded at a low scan rate to precisely measure the onset potential by evading the redox peak (1 mV/s). As shown in Fig. 4a, our 3D partially amorphous Au-Gd-Co_2B@TiO_2 catalyst reveal notably enhanced OER activity requiring an overpotential of only 260, 300, and 320 mV to attain a geometric activity of 100, 500, and 1000 mAcm^{-2} respectively in 1 M KOH, which is considerably lower than that of Gd-Co_2B@TiO_2, Gd-Co_3O_4@TiO2, and the benchmark IrO_2 anode. This OER performance is superior to that of the most noble metal catalyst in an alkaline electrolyte (Table S2). We inspected the different catalysts' redox behaviors by examining their polarization curve in the range of about 1.1–1.5 V vs. RHE. Interestingly, a slight positive shift in Co
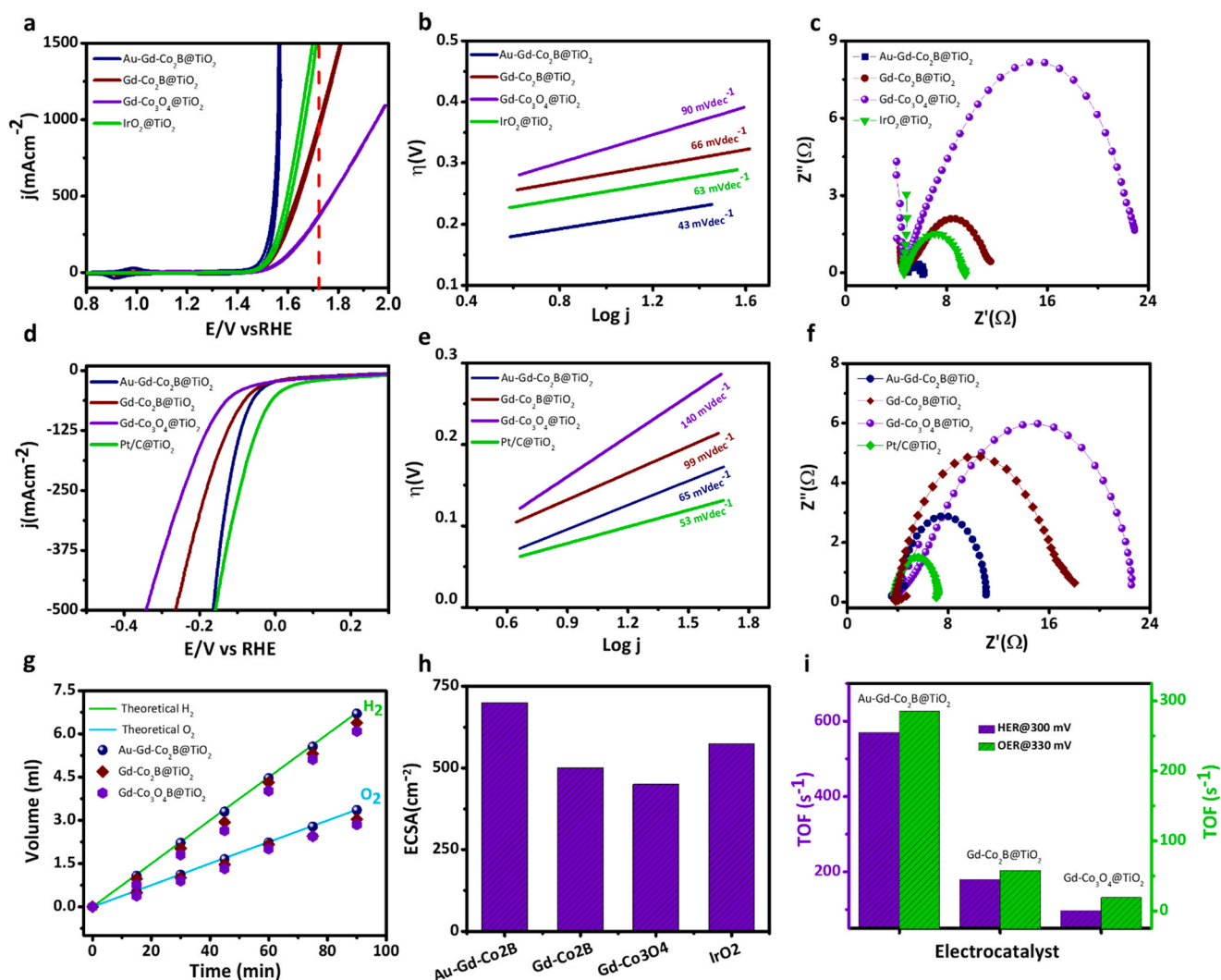

Fig. 4. Oxygen and hydrogen evolution catalysis in 1 M KOH. (a) OER polarization curve, the dotted red line represents the thermodynamic potential for hypochlorite formation, (b) corresponding Tafel plots, (c) EIS @ 1.5 V vs RHE, (d) HER polarization curve, (e) corresponding Tafel plots, (f) EIS @ −0.22 V vs RHE, (g) Faradic efficiency, (h) Electrochemical active surface area calculated from double layer capacitance and (i) Turn over frequency. (For interpretation of the references to color in this figure legend, the reader is referred to the web version of this article.)

oxidation peak was observed after Au incorporation that validated Co's partial oxidation (Fig. S17). These results demonstrate that highly electronegative Au atoms create abundant electrophilic Co sites that selectively bind with O-intermediates [41]. We also compared the OER activity of Au-Gd-Co$_2$B@TiO$_2$ with different mass loading of Gd-Co, and the one prepared with cathodic potential for 2 min, parades the highest OER activity (Fig. S18). The increment in overpotential with high mass loading is due to the stacking of Gd-Co$_2$B nanoflakes that decrease active sites' number and activity. The experimental findings demonstrated that Gd impurity has a considerable contribution to the overall activity of catalyst. The controlled Gd amount exponentially enhances the electrochemical performance in terms of high geometric activity and small overpotential for both OER and HER (Fig. S19).

The OER kinetics was evaluated by Tafel plots derived from the CV curve near onset potential. The Tafel slope value of Au-Gd-Co$_2$B@TiO$_2$ is only 43 mV dec^{-1} which is the smallest among these electrocatalysts, indicating favorable electrocatalytic kinetics and a higher transfer coefficient for the Au-Gd-Co$_2$B@TiO$_2$ electrode (Fig. 4b). Such lower Tafel slope (43 mVdec^{-1}) and significant inflation of current density within a small potential window ($\eta_{500} = 300$ mV and $\eta_{1000} = 320$ mV) place the Au-Gd-Co$_2$B@TiO$_2$ catalyst among the best recognized self-supported electrocatalyst. The OH adsorption on active sites initiates the water oxidation in alkaline electrolytes. Thus, the high affinity of catalysts for OH intermediates can indorse their development and equilibrium coverage. Hence succeeding step to desorb oxygen molecule will be the RDS and decrease the Tafel slope value [42]. The reduction in Tafel slope value after NaBH$_4$ treatment and Au loading is due to the coordination alteration and the development of electrophilic active sites (Au withdraw the electronic density from Co as evident from XPS and redox peaks) that trigger the electronic kinetics at the electrode-electrolyte junction. It was observed that boronization and Au loading enhance the OER kinetics and change the reaction pathway.

The Au incorporation and Gd-Co$_3$O$_4$ surface modification by boron can remarkably boost these electrocatalysts' conductivity, as demonstrated by the electrochemical impedance spectroscopy (EIS) results in Fig. 4c. The charge transfer resistance, obtained from the diameter of a circle (Nyquist plot) for Au-Gd-Co$_2$B@TiO$_2$ is 1.3 Ω, much smaller than, Gd-Co$_2$B@TiO$_2$ (9 Ω), Gd-Co$_3$O$_4$@TiO$_2$ (14 Ω) and IrO$_2$ (4.2 Ω) [16]. Such an improvement of conductivity after NaBH$_4$ treatment should be credited to the structural and surface tuning and the development of conductive Gd-Co$_2$B. The increment in Rct value after increasing the mass loading of Au supports our perspective that the optimum quantity of Au withdraws the electronic density from Co and vacates the active sites for the selective binding of OH-intermediate (Fig. S20).

To unveil the catalyst's intrinsic surface area activity and the probable reason for the enhanced OER activity of the Au-Gd-Co$_2$B@TiO$_2$ catalyst, we determined the electrochemically active surface area (ECSA) of different catalyst. Cyclic polarization curve was performed at different scan rates in non-faradic regions to estimate the double layer capacitance (C dl), which is proportional to the ECSA (Figs. S21 and S22a). As shown in Fig. 4h, among the four catalysts, our Au-Gd-Co$_2$B@TiO$_2$ catalyst has the largest ECSA, which is due to the amorphous features and oxygen defects created through the NaBH$_4$ treatment. After Au incorporation, a considerable enlargement in ECSA suggests that Au activates the Co-active sites and provides active centers for reaction intermediate. We further estimated the turnover frequency (TOF) from the ratio of oxygen production to the active metal sites determined from the metal redox area to evaluate the intrinsic activity (Fig. 4i) [21]. The high TOF of the Au-Gd-Co$_2$B@TiO$_2$ catalyst parades its highest instantaneous efficiency for water oxidation. This high inherent activity facilitates the optimum adsorption of OH intermediate at Au-Gd Co$_2$B interface, increases the rate of desorption of O$_2$ molecule, and vacates the electrochemically accessible active sites for the subsequent reaction. To further validate the plausible statement that metal doping with lower d electron increases the affinity of active sites for OH intermediate, faradic efficiency was measured using the water

displacement method (Fig. 4g) [43]. The high faradic efficiency of Au-Gd-Co$_2$B@TiO$_2$ supporting its selectivity for water oxidation. The high exchange current density (Io) further confirms that surface modification with B and Au incorporation inherently activates the active centers by increasing the number with optimum surface energy and coordination (Fig. S22b).

To find a promising cathode (HER catalyst) to integrate with our anode (Au-Gd-Co$_2$B@TiO$_2$) catalyst for complete water splitting, we evaluated the HER activity of different catalysts in 1 M KOH solution and compare the activity with benchmark catalyst (Pt/C). Interestingly, Au-Gd-Co$_2$B@TiO$_2$ shows excellent HER activity that is even better than that of benchmark Pt/C at high current density. The Au-Gd-Co$_2$B@TiO$_2$ reveals a low overpotential of 78 mV to attain a geometric activity of 100 mAcm^{-2}, which is pointedly inferior to the other samples (114 mV for Gd-Co$_2$B@TiO$_2$ and 164 mV for Gd-Co$_3$O$_4$@TiO$_2$) (Fig. 4d). We summarized the recently published HER electrocatalyst (Table S3), Au-Gd-Co$_2$B@TiO$_2$, has secured its position among the best catalyst. This superior performance demonstrates the low adsorption free energy of H* and admirable electronic conductivity of Au-Gd-Co$_2$B@TiO$_2$.

Fig. 4e shows that Au-Gd-Co$_2$B@TiO2 has a much lower Tafel slope of 65 mVdec^{-1}in comparison to the other catalyst (both Gd-Co$_2$B and Gd-Co$_3$O$_4$ have Tafel slope above 90 mV/dec), demonstrating that the unique Au-Gd-Co$_2$B@TiO$_2$ has an optimized electronic and surface structure which trigger the dissociation of the water molecule. The recent literature proposes that the water molecule combination with H* at cathodic potential results in the anomalous hydronium ion (H$_3$O$^+$) [44]. At high negative potential, deposited hydrogen forms hydrogen gas with the continuous flow of electrons. The H$_3$O$^+$ ions are then reduced to H* to complete the cycle. Gd-Co$_2$B and Gd-Co-Co$_3$O$_4$ Tafel slope shows that water dissociation is the rate-determining step (RDS) that requires a high potential to cross the energy barrier [45]. A high negative potential renders the formation of hydrogen gas directly instead of establishing H$_3$O$^+$ as an intermediate.

In contrast, the Tafel slope of Au-Gd-Co$_2$B@TiO$_2$ revealing that Heyrovsky, step is the RDS [45]. Subsequently, the hydronium ions are likely produced through an alternate water reduction mechanism during the alkaline HER. These results signpost that the Au-Gd-Co$_2$B interface eases water adsorption and declines H-adsorption, leading to the H$_3$O$^+$ formation near the electrode surface.

We then analyzed the OER and HER performance of the synthesized catalyst in an alkaline sea water-electrolyte (1 M KOH+ Seawater). As mentioned in the introduction section, the bottleneck challenge for alkaline seawater is the hypochlorite formation at overpotential above 480 mV, which will compete with water oxidation and severely hamper the proficiency of seawater electrolysis [2]. This catalyst (Au-Gd--Co$_2$B@TiO$_2$) needs only an overpotential of 330 mV to attain a high geometric activity (0.5 A/cm^2) in alkaline electrolyte, much lower than the equilibrium value (480 mV) to prevent the hypochlorite formation (Fig. 5a). We evaluated the corrosion resistance behavior of different catalysts in seawater by long-term immersion testing. Fig. S23 shows the well-preserved structural features of the Au-Gd-Co$_2$B@TiO$_2$ catalyst after ten days immersion experiment, and no structural collapse or corrosion pitting was observed. It was observed that without microwave treatment, Au NPs leach out from the sheets and dissolve in seawater, demonstrating that microwave heating creates a firm contact between Au NCs and Gd-Co$_2$B@TiO$_2$ sheets. Fig. 5c reveals the corrosion experiment performed in seawater for Au-Gd-Co$_2$B@TiO$_2$, Gd-Co$_2$B@TiO$_2$, Gd-Co$_3$O$_4$@TiO$_2$. The corrosion current density of Au-Gd-Co$_2$B@TiO$_2$ is much lower than Gd-Co$_2$B@TiO$_2$, and Gd-Co$_3$O$_4$@TiO$_2$, demonstrating that Au loading and metal-boride formation significantly enhance the corrosion resistance [46]. The high corrosion resistance and structural stability of Au-Gd-Co$_2$B@TiO$_2$ imply its viability for direct seawater electrolysis. As the water-splitting activity is deeply dependent on the amount of catalyst (catalyst loading), we have estimated the mass activity and specific activity (by normalizing the current density with ECSA) to probe the real activity of active sites. Fig. S24 shows the mass
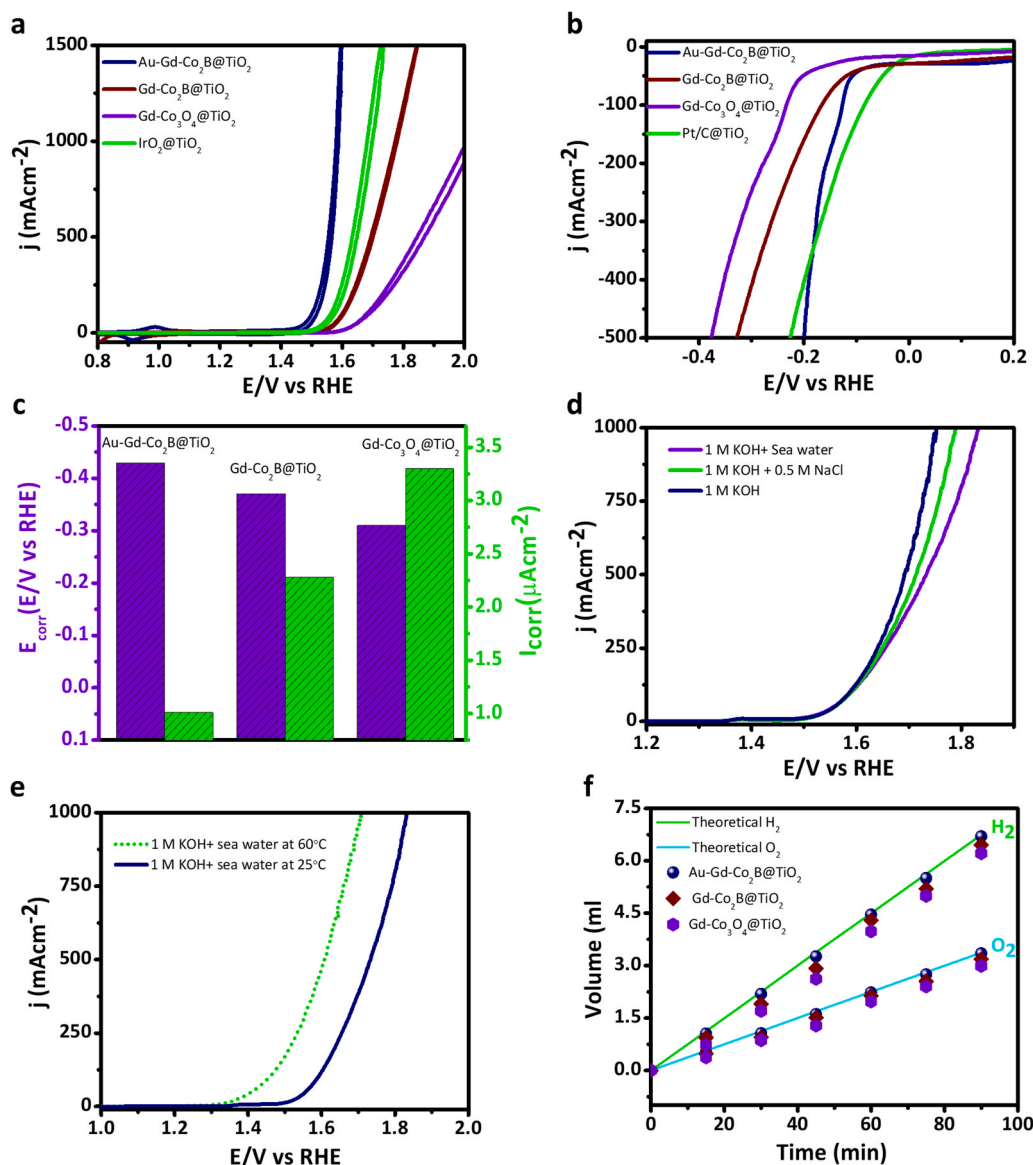
Fig. 5. (a) OER and (b) HER polarization curve in 1 M KOH alkaline sea water electrolyte, (c) Corrosion current density and corrosion potential in natural sea water, overall water splitting performance in 2 electrode setups with Au-Gd-Co2B@TiO2 as anode and cathode (d) in different electrolyte, and (e) at different temperature, and (f) faradic efficiency in natural sea water.

activity and specific activity comparison for all the synthesized catalysts at the same overpotential. The Au-Gd-Co$_2$B@TiO$_2$ has the highest mass and specific activity, indicating its most increased intrinsic activity.

As exhibited in Fig. 5a, Au-Gd-Co$_2$B@TiO$_2$ still shows excellent catalytic performance for OER, needing only 280 and 330 mV overpotential to attain a geometric activity of 100 and 500 mA/cm^2, respectively. However, all the catalyst parades slight decline due to the active site's blockage by Cl ions or due to insoluble precipitates that cover the electrode surface [46]. The OER performance of Au-Gd--Co$_2$B@TiO$_2$ in simulated seawater (1 M KOH + 1 M NaCl) is also evaluated; the activity is almost identical to that in the fresh 1 M KOH electrolyte (Fig. S25). However, a considerable increment in overpotential for Gd-Co$_2$B@TiO$_2$ demonstrates that Au doping with lower energy d electrons increases the selectivity of active sites for OH-intermediates; the slight decline in the efficiency is most probably due to the electrode surface coverage with insoluble precipitates [47]. The Tafel slope and charge transfer resistance value of these catalysts in different electrolytes are listed in Table S4 and reveal that the reaction kinetics, charge transfer rate, and charge transfer coefficient values are

slightly lowered in natural seawater. Even so, the Au-Gd-Co$_2$B@TiO$_2$ catalyst still delivers high geometric activity, and the demanded overpotential is only 360 mV for 1 A/cm^2, which is reasonably below 480 mV (potential needed to cause hypochlorite formation).

The Au-Gd-Co$_2$B@TiO$_2$ catalyst also shows good performance for HER in alkaline seawater electrolytes. The required overpotential is 194 mV for the current density of 500 mA/cm^2 (Fig. 5b). Based on the lower Tafel slope value, charge transfer resistance, and high geometric activity, it is well anticipated that Au-Gd-Co$_2$B@TiO$_2$ catalyst is active for OER and efficient for HER in sea water-electrolyte (Fig. 5).

Inspired by the outstanding electrochemical performance of the Au-Gd-Co$_2$B@TiO$_2$ catalyst, we further probed the water/seawater splitting efficiency by using a simple 2-electrodes setup, in which Au-Gd-Co$_2$B@TiO$_2$ is used as both anode and cathode. At low current density in 1 M KOH electrolyte, Au-Gd-Co$_2$B@TiO$_2$ needed a slightly higher overpotential than that for the benchmark Pt/C ‖ RuO$_2$ pair (Fig. S26a). However, this electrolyzer demonstrates outstanding seawater splitting performance at higher geometric activity in natural and simulated seawater electrolytes. As shown in Fig. 5d, at room temperature, the cell

voltage of only 1.65 and 1.68 V is required to drive a geometric activity of 500 mAcm^{-2} in simulated and natural seawater, respectively. This value is lower than the benchmark pair Pt/C ‖ RuO$_2$ and outperforms those of many bifunctional catalysts for alkaline freshwater splitting (Table S5). To enhance the large-scale practical application of this electrolyzer, the required potential is further reduced to 1.45 and 1.58 V for the geometric activity of 100 and 500 mAcm^{-2}, respectively, in natural alkaline seawater by increasing the electrolyte temperature to 60 °C (Fig. 5e). This temperature can be easily attained by using a solar thermal hot water system [48]. These values reveal the record-high performance of the Au-Gd-Co$_2$B@TiO$_2$ catalyst for overall seawater splitting.

We then measured the FE of the Au-Gd-Co$_2$B@TiO$_2$ and Gd-Co$_3$O$_4$@TiO$_2$ in alkaline seawater at room temperature by accumulating the evolved gaseous molecules over the anode (O$_2$) and cathode (H$_2$).

The molar ratio of O$_2$ and H$_2$ for Au-Gd-Co$_2$B@TiO$_2$ is close to 1:2, and the volume of gases measured agrees with the theoretical values, indicating an almost 100% faradic efficiency (98.2% for seawater) (Fig. 5f). However, a considerable reduction in FE for Gd-Co$_3$O$_4$ in alkaline seawater endorsed our statement that both Au incorporation and B modification considerably enhanced active sites' selectivity for -OH intermediate.

Operational stability is another crucial metric to evaluate the performance of an electrocatalyst. Fig. 6 revealed the outstanding durability of Au-Gd-Co$_2$B@TiO$_2$ for overall water splitting with no apparent decline over 200 h operations at a steady-state current density of 100 and 500 mAcm^{-2} in both natural and alkaline seawater electrolytes (Fig. 6c, d). An almost superimposed CV polarization curve before and after 1000th cycles further confirm the resistance of Au-Gd-Co$_2$B@TiO$_2$ catalyst against chemical and mechanical transformation (Fig. 6a, b)
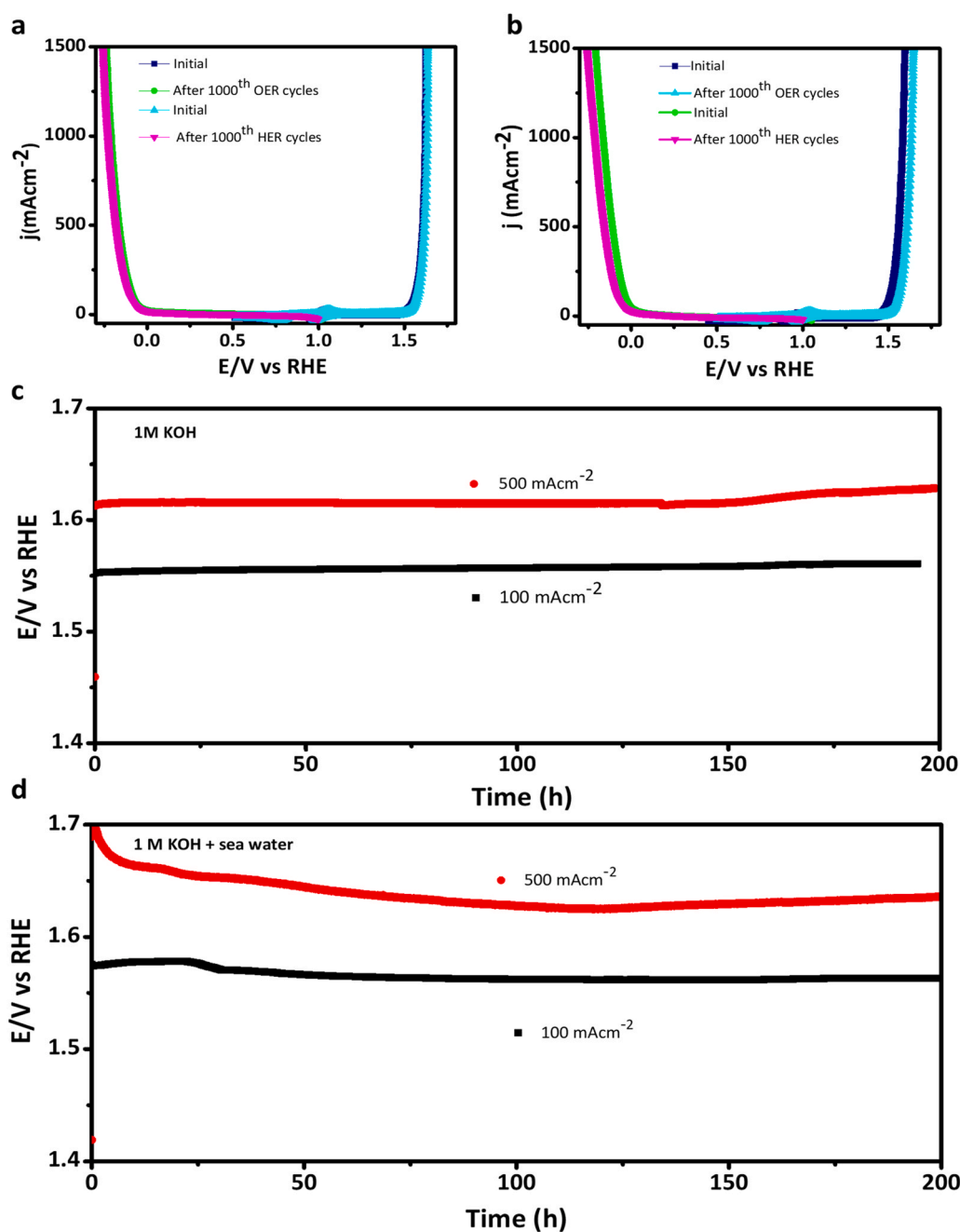

Fig. 6. OER and HER polarization curve of Au-Gd-Co$_2$B@TiO$_2$ before and after 1000th cycles in (a) 1 M KOH, (b) 1 M KOH seawater electrolyte, chronopotentiometry at 100 and 500 mAcm^{-2} in (c) 1 M KOH electrolyte and (d) 1 M KOH alkaline seawater electrolyte.

[38]. Interestingly, it was noticed that, without microwave treatment, Au NCs were leached out from the $Gd-Co_2B@TiO_2$ substrate after a short time of exposure in seawater at a high anodic potential (Fig. S26b). This observation demonstrates that microwave heating is crucial for strong interfacial interaction between Au NCs and support. Benefiting from the mechanical stability and excellent corrosion resistance, $Au-Gd-Co_2B@-TiO_2$ catalyst was also found stable for more than 200 h, even at a high geometric current (500 mA/cm^2) without noticeable fluctuation. It has been investigated that non-innocent impurities in natural seawater block the active sites, severely corrodes the anode surface by stress, pitting, and erosion-corrosion, and degrade the catalytic efficiency. Continuous current electrolysis was performed to probe the sustainability of $Au-Gd-Co_2B@TiO_2$ in natural seawater without filtration/purification. A small increment in the overpotential (17 mV) was observed compared to filtered seawater after 24 h of continuous electrolysis at 100 mAcm^{-2} (Fig. S27). These findings validate the anti-toxicity and corrosion resistance of $Au-Gd-Co_2B@TiO_2$ even at a high geometric activity. The long-term durability and selectivity of the $Au-Gd-Co_2B@TiO_2$ electrode show its potential for hydrogen production from actual seawater.

To probe the actual catalytically active sites for the outstanding OER performance of the $Au-Gd-Co_2B@TiO_2$ catalyst, we further examined its surface composition, topography, and chemical environment after a long-term OER experiment. The Fig. S28 shows the SEM images of the post chronopotentiometry catalyst. Even though some fissures can be noted on a macro scale, the overall nanocluster-nanoflakes embedded nanosheets structure is retained, reinforcing the corrosion resistance of the $Au-Gd-Co_2B@TiO_2$ catalyst. This observation indicates that the precipitates covered some portion of the catalyst surface [49]. Therefore, the catalyst with a high surface area containing many exposed active sites is crucial for natural seawater electrolysis. The corresponding TEM and HRTEM images reveal the homogenous distribution of Au NCs, the well-preserved amorphous structure of $Gd-Co_2B$ nanoflakes, and its intact with the underlying TiO_2 nanosheets (Fig. S29). The high-resolution XPS of B shows that B content was decreased from 10% to 8.7% due to intensive surface oxidation of catalyst. Also, the B 1s spectra show a characteristic peak at 191 eV, indicating boron oxo species' existence as detected in other metal borides [21]. The slight positive shift in the B.E of Co reveals that the Co surface was further oxidized to a higher valance state. The enhanced intensity of O 1s validates the high valance state of Co^{3+} after water oxidation (Fig. S30). By comparing the XPS analysis, it is evident that Au^0 is present before and after catalysis. However, after electrolysis, the Au^0 peak slightly shifts to the higher B.E. (Fig. S30b). Meanwhile, no reduction in the intensity of peak for Au^0 was observed, which indicates the retaining of original composition and periodic reshuffling of an electronic configuration for the sustained electrode process. However, without microwave treatment increase in the overpotential and decrease in the peak's intensity for Au in the XPS spectrum was observed that may be due to the structural/morphological rearrangements and leaching of highly soluble Au^{1+}, $^{3+}$ towards the electrolyte and thus reducing the numbers of accessible catalytic sites [50]. This observation was further strengthened to observe the decrease in the intensity of Au^0 peak and change in color of electrolyte due to the dissolution of Au. The persistent Au 4F XPS intensity, the color of electrolyte, and absence of Au content in electrolyte analyzed with ICP-OES for microwave treated sample validate our hypothesis that microwave treatment creates a strong interaction between nanosized Au and $Gd-Co_2B$ sheets.

The alkaline electrolyte after the OER test was inspected by Inductively coupled plasma optical emission spectroscopy. The results show the Au and boron-free electrolyte, indicating that B is the inherent part of the catalyst and cannot dissolve or leached out from the catalyst during the long-term experiment. The probable presence of hypochlorite products in the alkaline natural seawater electrolyte after the durability experiment was revealed using a colorimetric reagent. O-Tolidine was used as the indicator, and no change in color was observed (the electrolyte remains colorless) that endorse the 100% faradic efficiency (Fig. S31a). In addition, this electrolyte was further characterized by UV/VIS'S spectroscopy, and no peak was observed in the range of 400–500 nm. The absence of a characteristic absorption peak of hypochlorite (at 437 nm) mitigates the probability of hypochlorite formation (Fig. S31b) [46]. The $Au-Gd-Co_2B@TiO_2$ catalyst was also investigated with Time-of-flight secondary ion mass spectrometry (TOF-SIMS). Its high sensitivity allows the detection of dopants and surface impurities at a very low concentration level. The TOF-SIMS spectra of $Au-Gd-CoB@TiO_2$ demonstrate the characteristics peaks assigned to Co^+, CoO^+, $Co-OH^+$, $Co (OH)_2^+$ originates from the oxidized Co surface and Ti^+, $Ti-OH^+$, TiO_2^+ coming from the TiO_2 support [51]. These emissions unambiguously indicate the presence of hydroxyl groups on the catalyst surface. The spectra also show the characteristic peaks for B^+ and CoB that endorse the metal boride formation. A very intense peak at $m/z = 23$ and 39 corresponds to the Na^+ and NaOH incorporated during the synthesis of TiO_2 support. The absence of any peaks related to Cl products indorse the selectivity of $Au-Gd-Co_2B@TiO_2$ catalyst for seawater electrolysis (Figs. S32 and 33).

The electrochemical activity and post characterization results signpost the potential of $Au-Gd-Co_2B@TiO_2$ as a bifunctional self-supported catalyst for aggressive seawater splitting, and this outstanding performance can be attributed to the following factors. (I)The in-situ growth of highly branched TiO_2 nanosheets on Ti foil stabilizes the nanostructure, offers a large surface area for the nucleation and homogenous growth of active sites, and enhanced the intrinsic resistance of active sites against corrosive seawater. (II)The high electronic conduction in the Gd due to electrons of vacant 4f orbital could reside in the 5d orbital, turn into valance electrons, and optimize the coordination chemistry of active sites. (III) Due to the relativistic effect, the lower d orbitals of Au triggered Co's oxidation and enhanced its binding affinity for OH intermediates, leading to highly selective and terrific catalytic performance for seawater splitting. (IV) Microwave treatments create intense interfacial contact between Au NCs and $Gd-Co_2B$ hydrophilic surfaces and ensure the intimate contact of water molecules with the active sites. This contact ensures that the catalytic sites can always participate in catalysis by giving sufficient space for electrolyte diffusion and accelerating the kinetics of gas evolution from active sites. This heterogeneous catalyst has abundant active sites, fast kinetics, and a high transfer coefficient resulting from the B modification. This structural and surface optimization offers particular active sites for optimum adsorption-desorption of OH intermediates and Au-Co interface with high transfer coefficient, and conductivity makes it a potential contender against abrasive seawater.

3.4. Theoretical calculations

We performed theoretical calculations to inspect the impact of B modification and Au doping on the catalytic efficiency of IrO_2, $Gd-Co_3O_4@TiO_2$, $Gd-Co_2B@TiO_2$, and $Au-Gd-Co_2B@TiO_2$ for OER (Fig. S34). Different intermediates, i.e., M-OH, MO, MOOH, are formed on the active sites (adsorbate evolution mechanism) during the OER process. Fig. S35 shows the energy change profile for each intermediate. The theoretical overpotential of OER for $Gd-Co-Co_3O_4$ is 1.37 eV. The step M-OH to MO demonstrates the high energy barrier suggesting it is the RDS for OER. After B modification, the energy barrier for RDS is reduced to 1.17 eV, which signpost that B insertion creates the oxygen vacancies that trigger the OH adsorption on active sites. After Au doping, the energy barrier is substantially reduced to 0.77 eV and reveals higher intrinsic activity for OER. The Au insertion and its electronic contact with the $Gd-Co_2B$ nanoflakes change the reaction pathway, and now the step M-O to MOOH is the RDS as it reveals the largest energy barrier. These results envisage that B modification and Au incorporation to $Gd-Co_2B$ nanoflakes boost catalytic activity and selectivity.

4. Conclusion

We have developed a strategy to synthesize 3D self-supported Au-Gd-Co$_2$B@TiO$_2$ as an efficient bifunctional electrocatalyst for overall alkaline seawater splitting. The bimetallic boride structure with hydrophilic features is highly conductive and afford abundant active sites, ensuring high kinetics, fast charge transfer rate, and enhanced bubble released ability for seawater electrolysis. Its branched nanoflakes-nanosheets heterostructure offers a large surface area favorable for seawater diffusion and shields it from chloride anions corrosion. Additionally, its high selectivity for -OH intermediates from the Au doping (having lower energy d electrons) makes it eligible to work well in natural seawater conditions. With an optimized surface structure and metals ratio, the Au-Gd-Co$_2$B@TiO$_2$ anode needed a very low overpotential of 300 and 350 mV (much lower than the thermodynamic voltage of hypochlorite formation) to deliver a large geometric activity of 500 and 1000 mAcm^{-2} in actual alkaline seawater. In a two-electrode setup, Au-Gd-Co$_2$B@TiO$_2$ as an anode and cathode exhibit remarkable performance for overall seawater splitting and requires a record low voltage of 1.68 V to attain a geometric activity 1000 mAcm^{-2}. This electrolyzer also demonstrates higher stability at higher current density, small charge transfer resistance, high intrinsic kinetics, and TOF in alkaline seawater, superior to those of the Pt‖RuO$_2$ pair.

Supporting Information

Detailed methods (Material characterization and Electrochemical measurements), Additional SEM, TEM, AFM images, EDS spectrum, survey scan XPS, TOF-SIMs, electrochemical performance and comparison with the other reported results, Structure of OER intermediates and Schematics of the Gibbs free energy changes, SEM, TEM, HRTEM, TOF-SIMs after catalysis.

CRediT authorship contribution statement

Tanveer ul Haq: Conceptualization, Methodology, Investigation, Data curation, Validation, Formal analysis, Visualization, Writing – original draft. **Mujaheed Pasha**: Electron microscopy imaging. **Yongfeng Tong**: Performed XPS and TOF-SIMs. **Said A. Mansour**: Formal analysis. **Yousef Haik**: Formal analysis, review & editing, Resources, Supervision.

Declaration of Competing Interest

The authors declare that they have no known competing financial interests or personal relationships that could have appeared to influence the work reported in this paper.

Acknowledgements

Appendix A. Supporting information

Supplementary data associated with this article can be found in the online version at doi:10.1016/j.apcatb.2021.120836.

References

[1] T. Hibino, K. Kobayashi, M. Ito, M. Nagao, M. Fukui, S. Teranishi, Direct electrolysis of waste newspaper for sustainable hydrogen production: an oxygen-functionalized porous carbon anode, Appl. Catal. B Environ. 231 (2018) 191–199, https://doi.org/10.1016/j.apcatb.2018.03.021.

[2] W. Tong, M. Forster, F. Dionigi, S. Dresp, R. Sadeghi Erami, P. Strasser, A.J. Cowan, P. Farràs, Electrolysis of low-grade and saline surface water, Nat. Energy 5 (2020) 367–377, https://doi.org/10.1038/s41560-020-0550-8.

[3] S. Dresp, F. Dionigi, M. Klingenhof, P. Strasser, Direct electrolytic splitting of seawater: opportunities and challenges, ACS Energy Lett. 4 (2019) 933–942, https://doi.org/10.1021/acsenergylett.9b00220.

[4] R.K.B. Karlsson, A. Cornell, Selectivity between oxygen and chlorine evolution in the chlor-alkali and chlorate processes, Chem. Rev. 116 (2016) 2982–3028, https://doi.org/10.1021/acs.chemrev.5b00389.

[5] S. Wang, P. Yang, X. Sun, H. Xing, J. Hu, P. Chen, Z. Cui, W. Zhu, Z. Ma, Synthesis of 3D heterostructure Co-doped Fe2P electrocatalyst for overall seawater electrolysis, Appl. Catal. B Environ. 297 (2021), 120386, https://doi.org/10.1016/j.apcatb.2021.120386.

[6] L. Bigiani, D. Barreca, A. Gasparotto, T. Andreu, J. Verbeeck, C. Sada, E. Modin, O. I. Lebedev, J.R. Morante, C. Maccato, Selective anodes for seawater splitting via functionalization of manganese oxides by a plasma-assisted process, Appl. Catal. B Environ. 284 (2021), 119684, https://doi.org/10.1016/j.apcatb.2020.119684.

[7] G. Li, F. Li, Y. Zhao, W. Li, Z. Zhao, Y. Li, H. Yang, K. Fan, P. Zhang, L. Sun, Selective electrochemical alkaline seawater oxidation catalyzed by cobalt carbonate hydroxide nanorod arrays with sequential proton-electron transfer properties, ACS Sustain. Chem. Eng. 9 (2021) 905–913, https://doi.org/10.1021/acssuschemeng.0c07953.

[8] S. Gupta, M.K. Patel, A. Miotello, N. Patel, Metal boride-based catalysts for electrochemical water-splitting: a review, Adv. Funct. Mater. 121 (2020) 800, https://doi.org/10.1002/adfm.201906481.

[9] S. Gupta, M. Forster, A. Yadav, A.J. Cowan, N. Patel, M. Patel, Highly efficient and selective metal oxy-boride electrocatalysts for oxygen evolution from alkali and saline solutions, ACS Appl. Energy Mater. 31 (2020), 225208, https://doi.org/10.1021/acsaem.0c01040.

[10] J.A.D. del Rosario, G. Li, M.F.M. Labata, J.D. Ocon, P.Y.A. Chuang, Unravelling the roles of alkali-metal cations for the enhanced oxygen evolution reaction in alkaline media, Appl. Catal. B Environ. 288 (2021), 119981, https://doi.org/10.1016/j.apcatb.2021.119981.

[11] S. Zhao, R. Jin, H. Abroshan, C. Zeng, H. Zhang, S.D. House, E. Gottlieb, H.J. Kim, J.C. Yang, R. Jin, Gold nanoclusters promote Electrocatalytic water oxidation at the nanocluster/cose 2 interface, J. Am. Chem. Soc. 139 (2017) 1077–1080, https://doi.org/10.1021/jacs.6bl2529.

[12] A.L. Strickler, M. Escudero-Escribano, T.F. Jaramillo, Core-shell Au@metal-oxide nanoparticle electrocatalysts for enhanced oxygen evolution, Nano Lett. 17 (2017) 6040–6046, https://doi.org/10.1021/acs.nanolett.7b02357.

[13] X. Zhang, A. Chen, Z. Zhang, M. Jiao, Z. Zhou, Transition metal anchored C2N monolayers as efficient bifunctional electrocatalysts for hydrogen and oxygen evolution reactions, J. Mater. Chem. A 6 (2018) 11446–11452, https://doi.org/10.1039/c8ta03302a.

[14] H. Wang, Z.N. Chen, D. Wu, M. Cao, F. Sun, H. Zhang, H. You, W. Zhuang, R. Cao, Significantly enhanced overall water splitting performance by partial oxidation of Ir through Au modification in core-shell alloy structure, J. Am. Chem. Soc. 143 (2021) 4639–4645, https://doi.org/10.1021/jacs.0c12740.

[15] A. Nelson, Y. Zong, K.E. Fritz, J. Suntivich, R.D. Robinson, Assessment of soft ligand removal strategies: alkylation as a promising alternative to high-temperature treatments for colloidal nanoparticle surfaces, ACS Mater. Lett. 1 (2019) 177–184, https://doi.org/10.1021/acsmaterialslett.9b00089.

[16] T. Haq, Y. Haik, I. Hussain, H. Rehman, T.A. Al-ansari, Gd-doped Ni-oxychloride nanoclusters: new nanoscale electrocatalysts for high-performance water oxidation through surface and structural modification, ACS Appl. Mater. Interfaces 13 (2020) 468–479, https://doi.org/10.1021/acsami.0c17216.

[17] I.C. Man, H.Y. Su, F. Calle-Vallejo, H.A. Hansen, J.I. Martínez, N.G. Inoglu, J. Kitchin, T.F. Jaramillo, J.K. Nørskov, J. Rossmeisl, Universality in oxygen evolution electrocatalysis on oxide surfaces, ChemCatChem 121 (2011) 800, https://doi.org/10.1002/cctc.201000397.

[18] G. Qiu, S. Dharmarathna, Y. Zhang, N. Opembe, H. Huang, S.L. Suib, Facile microwave-assisted hydrothermal synthesis of CuO nanomaterials and their catalytic and electrochemical properties, J. Phys. Chem. C 116 (2012) 468–477, https://doi.org/10.1021/jp209911k.

[19] T. Ul Haq, Y. Haik, Y. Bicer, A. Munir, S. Mansour, Surface assembling of highly interconnected and vertically aligned porous nanosheets of Gd-CoB on TiO2 nanoflowers for durable methanol oxidation reaction, ChemCatChem 121 (2020) 800, https://doi.org/10.1002/cctc.202000392.

[20] L. Wu, L. Yu, Q. Zhu, B. McElhenny, F. Zhang, C. Wu, X. Xing, J. Bao, S. Chen, Z. Ren, Boron-modified cobalt iron layered double hydroxides for high efficiency seawater oxidation, Nano Energy 83 (2021), 105838, https://doi.org/10.1016/j.nanoen.2021.105838.

[21] T. Ul Haq, S.A. Mansour, A. Munir, Y. Haik, Gold-supported gadolinium doped CoB amorphous sheet: a new benchmark electrocatalyst for water oxidation with high turnover frequency, Adv. Funct. Mater. 1910309 (2020) 1–11, https://doi.org/10.1002/adfm.201910309.

[22] U.K. Sultana, J.D. Riches, A.P. O'Mullane, Gold doping in a layered Co-Ni hydroxide system via galvanic replacement for overall electrochemical water splitting, Adv. Funct. Mater. 28 (2018) 1–8, https://doi.org/10.1002/adfm.201804361.

[23] J. Zhang, H. Wang, L. Wang, S. Ali, C. Wang, L. Wang, X. Meng, B. Li, D.S. Su, F. S. Xiao, Wet-chemistry strong metal-support interactions in titania-supported Au catalysts, J. Am. Chem. Soc. 141 (2019) 2975–2983, https://doi.org/10.1021/jacs.8b10864.

[24] A. Kumar, Y. Kuang, Z. Liang, X. Sun, Microwave chemistry, recent advancements, and eco-friendly microwave-assisted synthesis of nanoarchitectures and their applications: a review, 100076-1025, Mater. Today Nano 11 (2020), https://doi.org/10.1016/j.mtnano.2020.100076.

[25] Y. Zhao, X. Jia, G. Chen, L. Shang, G.I.N. Waterhouse, L.Z. Wu, C.H. Tung, D. Ohare, T. Zhang, Ultrafine NiO nanosheets stabilized by TiO2 from monolayer NiTi-LDH precursors: an active water oxidation electrocatalyst, J. Am. Chem. Soc. 138 (2016) 6517–6524, https://doi.org/10.1021/jacs.6b01606.

[26] L. Wu, L. Yu, F. Zhang, B. McElhenny, D. Luo, A. Karim, S. Chen, Z. Ren, Heterogeneous bimetallic phosphide Ni2P-Fe2P as an efficient bifunctional catalyst for water/seawater splitting, Adv. Funct. Mater. 31 (2021) 1–12, https://doi.org/10.1002/adfm.202006484.

[27] S. Anantharaj, S. Noda, Amorphous catalysts and electrochemical water splitting: an untold story of harmony, Small 16 (2020) 1–24, https://doi.org/10.1002/smll.201905779.

[28] Q. Wu, M. Luo, J. Han, W. Peng, Y. Zhao, D. Chen, M. Peng, J. Liu, F.M.F. De Groot, Y. Tan, Identifying electrocatalytic sites of the nanoporous copper-ruthenium alloy for hydrogen evolution reaction in alkaline electrolyte, ACS Energy Lett. 5 (2020) 192–199, https://doi.org/10.1021/acsenergylett.9b02374.

[29] K. Wang, B. Liu, J. Li, X. Liu, Y. Zhou, X. Zhang, X. Bi, X. Jiang, In-situ synthesis of TiO2 nanostructures on Ti foil for enhanced and stable photocatalytic performance, J. Mater. Sci. Technol. 35 (2019) 615–622, https://doi.org/10.1016/j.jmst.2018.09.053.

[30] X. Liu, Q. Hu, B. Zhu, G. Li, L. Fan, X. Chai, Q. Zhang, J. Liu, C. He, Boosting electrochemical hydrogen evolution of porous metal phosphides nanosheets by coating defective TiO2 overlayers, Small 14 (2018) 1–8, https://doi.org/10.1002/smll.201802755.

[31] L. Wu, L. Yu, B. McElhenny, X. Xing, D. Luo, F. Zhang, J. Bao, S. Chen, Z. Ren, Rational design of core-shell-structured CoPx@FeOOH for efficient seawater electrolysis, Appl. Catal. B Environ. 294 (2021), 120256, https://doi.org/10.1016/j.apcatb.2021.120256.

[32] S. Xie, Y. Liu, J. Deng, J. Yang, X. Zhao, Z. Han, K. Zhang, H. Dai, Insights into the active sites of ordered mesoporous cobalt oxide catalysts for the total oxidation of o-xylene, J. Catal. 352 (2017) 282–292, https://doi.org/10.1016/j.jcat.2017.05.016.

[33] M.C. Biesinger, B.P. Payne, A.P. Grosvenor, L.W.M. Lau, A.R. Gerson, R.S.C. Smart, Resolving surface chemical states in XPS analysis of first row transition metals, oxides and hydroxides: Cr, Mn, Fe, Co and Ni, Appl. Surf. Sci. 257 (2011) 2717–2730, https://doi.org/10.1016/j.apsusc.2010.10.051.

[34] L. Liu, Z. Jiang, L. Fang, H. Xu, H. Zhang, X. Gu, Y. Wang, Probing the crystal plane effect of Co3O4 for enhanced electrocatalytic performance toward efficient overall water splitting, ACS Appl. Mater. Interfaces 9 (2017) 27736–27744, https://doi.org/10.1021/acsami.7b07793.

[35] W. Lu, T. Liu, L. Xie, C. Tang, D. Liu, S. Hao, F. Qu, G. Du, Y. Ma, A.M. Asiri, X. Sun, In situ derived Co-B nanoarray: a high-efficiency and durable 3D bifunctional electrocatalyst for overall alkaline water splitting, Small 13 (2017) 1–8, https://doi.org/10.1002/smll.201700805.

[36] S. Gupta, N. Patel, A. Miotello, D.C. Kothari, Cobalt-Boride: an efficient and robust electrocatalyst for Hydrogen Evolution Reaction, J. Power Sources 279 (2015) 620–625, https://doi.org/10.1016/j.jpowsour.2015.01.009.

[37] H.B. Tao, L. Fang, J. Chen, H. Bin Yang, J. Gao, J. Miao, S. Chen, B. Liu, Identification of surface reactivity descriptor for transition metal oxides in oxygen evolution reaction, 9978-85, J. Am. Chem. Soc. 138 (2016), https://doi.org/10.1021/jacs.6b05398.

[38] T.U. Haq, Y. Haik, I. Hussain, H.U. Rehman, T.A. Al-Ansari, Gd-doped Ni-oxychloride nanoclusters: new nanoscale electrocatalysts for high-performance water oxidation through surface and structural modification, ACS Appl. Mater. Interfaces 13 (2021) 468–479, https://doi.org/10.1021/acsami.0c17216.

[39] M. De Anda Villa, J. Gaudin, D. Amans, F. Boudjada, J. Bozek, R. Evaristo Grisenti, E. Lamour, G. Laurens, S. Macé, C. Nicolas, I. Papagiannouli, M. Patanen, C. Prigent, E. Robert, S. Steydli, M. Trassinelli, D. Vernhet, A. Lévy, Assessing the surface oxidation state of free-standing gold nanoparticles produced by laser ablation, Langmuir 35 (2019) 11859–11871, https://doi.org/10.1021/acs.langmuir.9b02159.

[40] Y. Bai, M. Sekita, M. Schmid, T. Bischof, H.P. Steinrück, J.M. Gottfried, Interfacial coordination interactions studied on cobalt octaethylporphyrin and cobalt tetraphenylporphyrin monolayers on Au(111), 4336-44, Phys. Chem. Chem. Phys. 12 (2010), https://doi.org/10.1039/b924974p.

[41] X. Lu, Y.H. Ng, C. Zhao, Gold nanoparticles embedded within mesoporous cobalt oxide enhance electrochemical oxygen evolution, ChemSusChem 7 (2014) 82–86, https://doi.org/10.1002/cssc.201300975.

[42] A. Chunduri, S. Gupta, O. Bapat, A. Bhide, R. Fernandes, M.K. Patel, V. Bambole, A. Miotello, N. Patel, A unique amorphous cobalt-phosphide-boride bifunctional electrocatalyst for enhanced alkaline water-splitting, Appl. Catal. B Environ. 259 (2019), 118051, https://doi.org/10.1016/j.apcatb.2019.118051.

[43] A. Munir, T. Ul Haq, M. Saleem, A. Qurashi, S.Z. Hussain, F. Sher, A. Ul-Hamid, A. Jilani, I. Hussain, Controlled engineering of nickel carbide induced N-enriched carbon nanotubes for hydrogen and oxygen evolution reactions in wide pH range, Electrochim. Acta 341 (2020), 136032, https://doi.org/10.1016/j.electacta.2020.136032.

[44] R. Miao, B. Dutta, S. Sahoo, J. He, W. Zhong, S.A. Cetegen, T. Jiang, S.P. Alpay, S. L. Suib, Mesoporous iron sulfide for highly efficient electrocatalytic hydrogen evolution, J. Am. Chem. Soc. 139 (2017) 13604–13607, https://doi.org/10.1021/jacs.7b07044.

[45] J. Chen, G. Liu, Y.Z. Zhu, M. Su, P. Yin, X.J. Wu, Q. Lu, C. Tan, M. Zhao, Z. Liu, W. Yang, H. Li, G.H. Nam, L. Zhang, Z. Chen, X. Huang, P.M. Radjenovic, W. Huang, Z.Q. Tian, J.F. Li, H. Zhang, Ag@MoS2 core-shell heterostructure as SERS platform to reveal the hydrogen evolution active sites of single-layer MoS2, J. Am. Chem. Soc. 142 (2020) 7161–7167, https://doi.org/10.1021/jacs.0c01649.

[46] J. Li, Y. Liu, H. Chen, Z. Zhang, X. Zou, Design of a multilayered oxygen-evolution electrode with high catalytic activity and corrosion resistance for saline water splitting, Adv. Funct. Mater. 2101820 (2021) 1–9, https://doi.org/10.1002/adfm.202101820.

[47] X. Lu, J. Pan, E. Lovell, T.H. Tan, Y.H. Ng, R. Amal, A sea-change: manganese doped nickel/nickel oxide electrocatalysts for hydrogen generation from seawater, Energy Environ. Sci. 11 (2018) 1898–1910, https://doi.org/10.1039/c8ee00976g.

[48] T. Ma, M. Li, A. Kazemian, Photovoltaic thermal module and solar thermal collector connected in series to produce electricity and high-grade heat simultaneously, Appl. Energy 261 (2020), 114380, https://doi.org/10.1016/j.apenergy.2019.114380.

[49] L. Yu, L. Wu, S. Song, B. McElhenny, F. Zhang, S. Chen, Z. Ren, Hydrogen generation from seawater electrolysis over a sandwich-like NiCoN=NixP|NiCoN microsheet array catalyst, ACS Energy Lett. 5 (2020) 2681–2689, https://doi.org/10.1021/acsenergylett.0c01244.

[50] O. Diaz-Morales, F. Calle-Vallejo, C. De Munck, M.T.M. Koper, Electrochemical water splitting by gold: evidence for an oxide decomposition mechanism, Chem. Sci. 4 (2013) 2334, https://doi.org/10.1039/c3sc50301a.

[51] S. Chenakin, N. Kruse, Combining XPS and ToF-SIMS for assessing the CO oxidation activity of Au/TiO2 catalysts, J. Catal. 358 (2018) 224–236, https://doi.org/10.1016/j.jcat.2017.12.010.